

Hydride Ion as a Two-Electron Donor in a Nanoporous Crystalline Semiconductor $12\text{CaO}\cdot 7\text{Al}_2\text{O}_3$

Katsuro Hayashi,^{*,†} Peter V. Sushko,[§] Alexander L. Shluger,[§] Masahiro Hirano,[†] and Hideo Hosono^{†,‡}

Frontier Collaborative Research Center and Materials and Structures Laboratory, Tokyo Institute of Technology, S2-13, 4259 Nagatsuta, Yokohama 226-8503, Japan, and Department of Physics and Astronomy, University College London, Gower St., London WC1E 6BT, United Kingdom

Received: July 19, 2005; In Final Form: September 1, 2005

The $12\text{CaO}\cdot 7\text{Al}_2\text{O}_3$ (C12A7) crystal with a nanoporous lattice framework exhibits high electrical conductivity with an activation energy of ~ 1.5 eV when equilibrated in a hydrogen atmosphere above ~ 800 °C. The high conductivity is preserved in a quenched state below ~ 600 °C with a reduced activation energy of ~ 0.8 eV. Such complex behavior in electrical conductivity is associated with incorporation of hydride ions (H^-) in cages of the lattice framework. Electromotive force measurements reveal that the major carrier for the conductivity is electron with a small contribution by proton (H^+), ruling out the possibility of direct intercage migration of the H^- ion. A combination of these observations with the *ab initio* calculations leads to the conclusion that the electrons are thermally generated from the H^- ion by the dissociation into two electrons and an proton, which is further converted to an OH^- ion via reaction with an extraframework oxide ion (O^{2-}). The energy difference between the initial ($\text{H}^- + \text{O}^{2-}$) and the final ($2\text{e}^- + \text{OH}^-$) states as evaluated by the theoretical calculation is as small as ~ 1 eV, which agrees well with an experimentally obtained enthalpy change, ~ 1.4 eV. Thus, internal equilibration between the extraframework hydrogen and the oxygen species is responsible for the thermal generation of the carrier electron. It is also suggested that the same conductive ($2\text{e}^- + \text{OH}^-$) state is reached by the photoirradiation of H^- -containing C12A7. In this case the photoionization of H^- forms an electron and an H^0 atom, which then forms an OH^- ion and another electron with thermal assistance. The persistence of photoinduced conductivity is explained by the slow kinetics of the reverse process at room temperature.

Introduction

Hydrogen is an unusual chemical species whose charge can vary from negative to positive depending on the environment provided by host materials. Interconversion of hydrogen charge states, including H^+ (proton), H^0 (atomic hydrogen), and H^- (hydride ion), can be induced by simply transferring an electron. However, these species behave quite differently from each other and provide novel functions in various materials. For example, hydrogen serves as an amphoteric dopant in semiconductors,¹ a fast diffusing species in proton-conducting oxides,² a dangling bond passivator in amorphous silicon,³ and a neutral solute in hydrogen-storage materials.⁴ Understanding the static and dynamic properties of each species and achieving control over them is crucial for the development of innovative materials, particularly for the hydrogen economy. Although the properties of protons in metal oxides are relatively well-understood, H^- ions have been identified or suggested only in a limited class of oxide materials.^{5–15} This is because the formation of H^- ions generally requires strong reducing conditions, which often result in degradation of the host material itself. Despite little being known about the behavior of H^- ions in oxides, they are of interest for their role in designing materials with novel

physical^{10–13} and transport properties.¹⁴ In this study, we focus on a nanoporous crystal $12\text{CaO}\cdot 7\text{Al}_2\text{O}_3$ (C12A7) doped with hydrogen in the form of H^+ and H^- .¹¹

Figure 1 shows the crystal structure of C12A7. The composition of the stoichiometric unit cell $2(\text{Ca}_{12}\text{Al}_{14}\text{O}_{33})$ may be expressed as $[\text{Ca}_{24}\text{Al}_{28}\text{O}_{64}]^{4+} + 2\text{O}^{2-}$. The first part describes a positively charged three-dimensional lattice framework formed by 12 cages with an inner diameter of 0.4 nm. Thus, a mean effective charge of $+1/3$ ($= +4/12$) is allocated to each cage. The remaining two extraframework O^{2-} ions are randomly distributed in the crystal framework.¹⁶ The positive charge of the lattice framework and the appropriate size of the cage facilitate the incorporation of extrinsic extraframework anions as a substitute for the O^{2-} ions by appropriate treatment. Non-hydrogenous extraframework anions reported so far are F^- , Cl^- ,¹⁷ S^{2-} ,¹⁸ O_2^- ,^{19–24} O^- ,^{20–23} and O_2^{2-} .²⁵ In addition, severe reducing of C12A7 causes deficiency in extraframework anions, resulting in incorporation of electrons in cages.²⁶ Theoretical calculation demonstrated that the electron density locates within the cage,^{27,28} thus electrons also may be regarded as extrinsic extraframework anions in the broad sense.

The three-dimensional nanoporous structure of C12A7 further provides conduction pathways for the extraframework ions and electrons. For example, in an oxidizing or inert gas atmosphere, C12A7 exhibits a high oxide ion conductivity (see Figure 2A), which is only 8–10 times less than that of yttria-stabilized

* Address correspondence to this author. E-mail: k-hayashi@lucid.msl.titech.ac.jp.

[†] Frontier Collaborative Research Center.

[‡] Materials and Structures Laboratory.

[§] University College London.

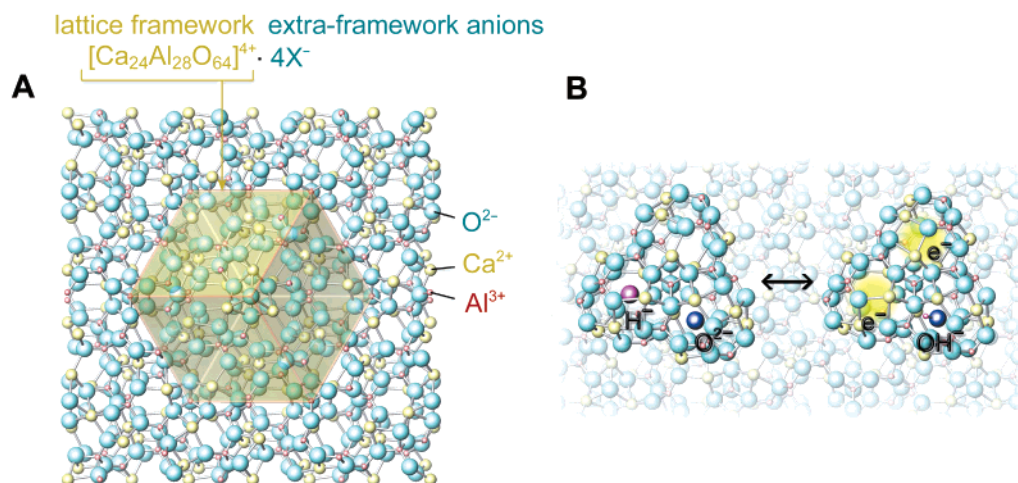


Figure 1. Crystal structure of $12\text{CaO} \cdot 7\text{Al}_2\text{O}_3$. (A) Structure of the lattice framework viewed along the $\langle 111 \rangle$ direction. The yellow frame indicates the cubic unit cell, $[\text{Ca}_{24}\text{Al}_{28}\text{O}_{64}]^{4+}$, with the lattice constant of 1.199 nm. Extraframework species are omitted for simplicity in this figure. (B) Extraframework species relevant to this study. Two-electron generation from a pair of H^- and O^{2-} ions is schematically shown.

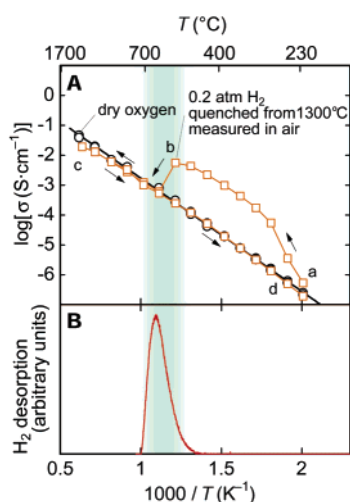


Figure 2. Effect of H^- incorporation on the electrical conductivity. (A) Bulk electrical conductivity in C12A7. Open black circles show the oxide ion conductivity of C12A7 measured in dry oxygen. Open orange squares show conductivity of the sample equilibrated at 1300 $^\circ\text{C}$ in 0.2 atm hydrogen atmosphere and quenched to room temperature. The measurements were made in air along the path $a \rightarrow d$. The electrical conductivity dropped to the level of the oxide ion conduction above ~ 600 $^\circ\text{C}$ (point b), which is the onset temperature of hydrogen desorption (see panel B below). (B) Evolved gas analysis of C12A7 loaded with H^- ions. Heating rate was 10 $\text{K} \cdot \text{min}^{-1}$.

zirconia with a transference number of unity.²⁹ The extraframework O^{2-} ions are believed to be the mobile species in the oxide ion conductivity.³⁰ When the extraframework electrons are injected into C12A7, their cage-to-cage hopping motion yields electronic conduction.^{27,28}

As for hydrogenous anions, the formation of OH^- ^{31,32} and H^- ^{11,12,33} has been found so far. H^+ in the form of OH^- is easily detected and quantified by infrared spectroscopy³² while the presence of H^- is suggested on the basis of the previously reported ultraviolet (UV) light-induced¹¹ and electron beam-induced¹² conversion of hydrogen-treated C12A7 from an insulator to a conductor, and H^- ion emission into vacuum by an electric field extraction.¹³ The existence of H^- species is further supported by theoretical calculations.³⁴ Recently, an electron paramagnetic spin resonance (EPR) study on the hydrogen-treated C12A7 at low temperatures³⁵ provided additional evidence of the presence of H^- ions. The hydrogen-treated C12A7 in the as-prepared state has shown no paramag-

netic centers in these experiments. However, when illuminated with UV-light at 4 K, nearly equal amounts of H^\bullet atoms and electrons were detected by the EPR, indicating that the non-paramagnetic H^- ions present in the as-prepared C12A7 were photodissociated into H^\bullet and electrons.³⁴ Concentrations of both species were gradually reduced by heating. The H^\bullet signal was completely lost after heating the sample to 100 K, while approximately half of the initially formed electrons survived up to room temperature. These facts further indicate that (i) H^- can act as an electron source, (ii) H^\bullet remains stable only at very low temperatures, and (iii) persistence of the H^- -derived electrons at room temperature is associated with oxidation of H^- ions to a nonparamagnetic state, i.e., H^+ or H_2 .

The purpose of this study is to elucidate how the H^- ion in C12A7 contributes to transport properties at elevated temperatures. This is explored by high-temperature electrical conductivity measurements. It is demonstrated that the presence of H^- ions in the cage is crucial for a high level of electrical conduction. Ab initio calculations are also employed to elaborate on the electrical conductivity mechanisms at an atomistic level.

Experimental Section

Electrical Conductivity Measurement. High-density polycrystalline C12A7 disks with a relative density of more than 99% were fabricated as described in ref 36. A Pt paste was applied to both surfaces of disks and sintered at 1000 $^\circ\text{C}$ to form porous Pt electrodes. These disks were equilibrated for 2–48 h at temperatures between 820 and 1300 $^\circ\text{C}$ in a 0.2 atm hydrogen atmosphere ($p(\text{H}_2) = 0.2$ atm, $p(\text{H}_2\text{O}) = 5 \times 10^{-4}$ atm, balance N_2) and then quenched to room temperature. Steam partial pressure, $p(\text{H}_2\text{O})$, was controlled with a humidifier and measured with a dew point meter. Resultant samples were mounted on a spring-loaded alumina support, which was inserted in an alumina tube furnace. The temperature dependence of electrical conductivity was measured by 4-probe impedance spectroscopy in a cycle of heating or cooling at a rate of 10 $\text{K} \cdot \text{min}^{-1}$ followed by holding for 10 min, and the ac frequency sweeping for 10 min in both the 0.2 atm hydrogen and air atmospheres. The equilibrium conductivity at >800 $^\circ\text{C}$ in the 0.2 atm hydrogen was measured after keeping the sample at each measurement temperature for 2–48 h. The oxide ion conductivity was measured in dry oxygen ($p(\text{O}_2) = 1$ atm, $p(\text{H}_2\text{O}) < 5 \times 10^{-4}$ atm) after pretreatment of the samples in the same atmosphere at 1350 $^\circ\text{C}$.

Emf Measurement. The C12A7 disk with porous Pt electrodes was inserted between two alumina tubes with intervening Pt ring gaskets, and the assembly was annealed at 1300 °C in a hydrogen atmosphere under a weight load to provide gastightness. The emf was measured in a hydrogen concentration cell with a voltmeter with a flowing gas mixture of either ($p(\text{H}_2) = 0.2 \text{ atm}$, $p(\text{H}_2\text{O}) = 1 \times 10^{-3} \text{ atm}$) or ($p(\text{H}_2) = 1 \text{ atm}$, $p(\text{H}_2\text{O}) = 5 \times 10^{-3} \text{ atm}$) in each compartment. Under these conditions, the cell voltage is given by $RT/2F\{t(\text{H}^+) - t(\text{H}^-)\} \ln 5$, where R , F , $t(\text{H}^+)$, and $t(\text{H}^-)$ are the gas constant, the Faraday constant, and the transference numbers for proton and hydride ions, respectively. To check the accuracy of the measurement, gases fed to two compartments were exchanged by using a four-way valve. The emf was measured before and after the reversal of gases.

Characterization of Hydrogen. Evolved gas analysis was conducted for polycrystalline C12A7 quenched at 1300 °C in the hydrogen atmosphere with use of a Rigaku Thermoplus TG-MS system. The intensity of evolved H_2 was measured with a quadrupole mass spectrometer during a heating with $10 \text{ K} \cdot \text{min}^{-1}$ in a He gas flow.

Single crystals³⁷ treated under the same conditions as those for the electrical conductivity measurements were used to evaluate the OH^- concentration from the infrared optical absorption band at 3560 cm^{-1} (molar extinction coefficient at peak top: $14.8 \text{ dm}^3 \cdot \text{cm}^{-1} \cdot \text{mol}^{-1}$ ³²). Raman spectroscopy of single crystals at the range $4100\text{--}4400 \text{ cm}^{-1}$ was also conducted to confirm the absence of H_2 molecules.

UV-Light Irradiation. Both sides of the hydrogen-treated single crystals were irradiated with UV-light, using a Xe-lamp at room temperature for 1 day as a accumulated duration. The light component with wavelength longer than 320 nm was cut with use of a dichroic mirror and a color glass filter. Energy density of irradiated light on the sample was $\sim 100 \text{ mW cm}^{-2}$. Concentration of the extraframework electrons was evaluated from the 2.8 eV band intensity by using the relationship obtained in ref 26. Saturation in the electron formation was confirmed by observing the intensity change of the 2.8 eV band against irradiation time.

Theoretical Calculations. An embedded cluster approach that combines a quantum-mechanical treatment of a “region of interest” and a classical treatment of the rest of the system was used in this study. This technique, implemented in the computer code Guess, has been thoroughly described in refs 38 and 39, and tested in defect studies of several oxides.^{27,28,38,39} In brief, the C12A7 is represented by using a large nearly spherical nanocluster containing over 7500 atoms. The nanocluster is divided into a spherical region I, containing nearly 700 atoms, and the remaining part, region II. Region I includes a cluster considered quantum-mechanically (QM cluster), a classically considered region that surrounds the QM cluster and the interface between them. Atoms in region II are represented by using classical interatomic potentials. The total energy of the system is minimized with respect to the coordinates of all atoms in region I. Atoms in region II are fixed; they provide the correct boundary conditions for region I. This approach allows one to consider complex crystalline and amorphous materials as well as to study different charge states of defects and to account accurately for defect-induced lattice polarization. In particular, in the case of C12A7, we consider explicitly the intrinsic disorder induced by the presence of the extraframework O^{2-} ions and account for a large lattice relaxation induced by these O^{2-} ions as well as by trapped electrons. In addition, the method allows one to use a variety of methods for electronic structure

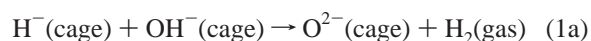
calculations including hybrid density functionals (e.g., B3LYP) which contain a contribution of the exact exchange interaction.

The QM cluster is built of two adjacent framework cages (2-cage cluster) and includes 54 atoms; the interface region between the quantum-mechanical and classical regions includes a further 87 atoms while the remaining atoms are considered classically. Calculations were made with the B3LYP density functional and the 6-31G basis set for anions and lanl2dz basis sets for cations.⁴⁰ A linear interpolation approach was used to examine the energy barrier for migration of hydrogen species. In this approach \mathbf{R}_1 and \mathbf{R}_2 define coordinates of all atoms for configurations of the hydrogen species occupying cages 1 and 2, respectively. The initial pathway for the diffusion was estimated by using $\mathbf{R}(t) = t \times \mathbf{R}_1 + (t - 1) \times \mathbf{R}_2$, where t is a parameter: $0 < t < 1$. Then the adiabatic potential for the diffusion was built by calculating energies for several images $\mathbf{R}(t)$, where all degrees of freedom but one were explicitly relaxed for each t . This procedure is useful for calculations of adiabatic migration pathways in systems with a large number of degrees of freedom.

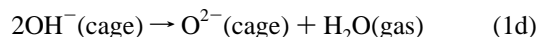
Results

Electrical Conductivity. The orange squares in Figure 2A show the change in electrical conductivity for the sample, which was annealed in a hydrogen atmosphere at 1300 °C and then quenched, measured during the heating from room temperature to 1300 °C and the subsequent cooling to room temperature in air. During heating, its conductivity is ~ 1.5 orders of magnitude larger than that of oxide ions in an oxygen-treated sample until $\sim 600 \text{ °C}$ (point “b”). It then follows the oxide ion conductivity after a drop at $\sim 600 \text{ °C}$. Figure 2B shows the desorption of H_2 gas during heating in helium gas. The abrupt conductivity change at $\sim 600 \text{ °C}$ (Figure 2A) correlates well with the desorption of H_2 in this temperature range (Figure 2B). Thus, it is concluded that the excess conductivity observed between points a and b in Figure 2A originates from the hydrogen incorporated in the sample.

Since neither molecular hydrogenous species by Raman spectroscopy nor H^\bullet by EPR^{11,35} was detected in the hydrogen-treated samples, the precursor for the H_2 molecules desorbed at 600 °C was ascribed to encaged H^- ions and/or protons in the form of OH^- ions. Provided that the H_2 gas-desorption is accompanied by no electron formation in the cages, the desorption process is described by one of following three reactions or their combinations:



Absence of electron formation will be validated in the discussion section. H_2 gas formed via reaction 1a is derived only from extraframework anions, while reactions 1b and 1c involve O_2 and H_2O gases, which are initially included in the He carrier gas as impurities and/or emitted from the electronic furnace for the evolved gas analysis. Reactions shown in eqs 1a–c link the H_2 desorption with the decrease in the concentration of H^- ions. This suggests that the drop of the conductivity at point b (see Figure 2A) is due to annihilation of the H^- species. We also note that the H_2 desorption cannot be associated with the dehydration reaction:



because the H_2 desorption temperature is much lower than the dehydration temperature ($\sim 1000^\circ\text{C}$) in the helium atmosphere.³²

The electrical conductivity was also measured for samples in equilibrium with the hydrogen atmosphere at $>800^\circ\text{C}$ and for samples that were first equilibrated in the hydrogen atmosphere at 1300°C or 1125°C and then quenched. These results are plotted in Figure 3A. The equilibrium conductivity indicated by the green line is ~ 1.5 orders of magnitude larger than the oxide ion conductivity at 1300°C and exhibits an activation energy, ΔH_{h} , of 1.47 eV (Figure 3B).

To determine the types of carriers contributing to such a high conductivity, electromotive force (emf) measurements with a hydrogen concentration cell were carried out over the temperature range $800\text{--}1300^\circ\text{C}$. Figure 4 shows temperature change in proton transference number, i.e., the ratio of proton conductivity to the total one. A very small value in the transference number (~ 0.01) indicates that an electron is the dominant charge carrier with a transference number of almost unity. Partial proton conductivity estimated from the transference number was $\sim 1 \times 10^{-2}\text{ S}\cdot\text{cm}^{-1}$ at 1300°C , while electronic conductivity was as high as $\sim 1\text{ S}\cdot\text{cm}^{-1}$. No H^- contribution to the total conductivity was observed within the accuracy of our experiment. Hence, it is evident that the high conductivity observed at $>800^\circ\text{C}$ is not due to a direct migration of H^- ions.

As shown in Figure 3A, the conductivity of the quenched samples at temperatures below $\sim 600^\circ\text{C}$ becomes larger with an increase in the quenching temperature. As indicated by dashed lines in Figure 3A, extrapolation to high temperatures reveals that the conductivities in the quenched states agree with the equilibrium conductivities at the corresponding quenching temperatures. Similar behavior was reported for samples annealed at 800°C in a $5\%\text{ H}_2\text{--}95\%\text{ N}_2$ atmosphere and then quenched to lower temperatures.⁴¹ The observed correlation between the equilibrium and the quenched states suggests that the equilibrium distribution of extraframework species in the sample in a hydrogen atmosphere at $>800^\circ\text{C}$ is “frozen-in” by the quenching and is preserved until the sample is heated to the hydrogen effusion temperature of $\sim 600^\circ\text{C}$. The correlation further indicates that the electrons are the dominant charge carriers in the quenched state, the same as in the high-temperature equilibrium. As indicated in Figure 3B, the apparent activation energy, ΔH_{q} , for the conductivity in the quenched states is $0.76\text{--}0.86\text{ eV}$. Since the activation energy for the electron migration, ΔH_{m} , has been estimated to be $0.1\text{--}0.2\text{ eV}$ both experimentally^{11,33} and theoretically,^{27,28} the apparent activation energy, ΔH_{e} , for the carrier electron formation is $\sim 0.7\text{ eV}$ from the relationship $\Delta H_{\text{q}} = \Delta H_{\text{m}} + \Delta H_{\text{e}}$.

Theoretical Calculations. The experimental observations have been corroborated by ab initio calculations. The calculated electronic structure of H^- is shown in Figure 5A. The H^- energy level is located approximately 1.1 eV above the top of the valence band.³⁴ The two electrons of H^- occupy an s-like state well localized within one cage (cage 2) of the 2-cage QM cluster, while the other cage (cage 1) is unoccupied. A linear interpolation approach was used to examine the energy barrier for the direct intercage migration of H^- . The calculated barrier for H^- diffusion is 2.8 eV , which is much higher than the observed activation energy of the conductivity in the quenched states, $0.86\text{--}0.76\text{ eV}$, which rules out the possibility of H^- conduction in this system.

The H^- ion in C12A7, as the only species that can give rise to the conduction electrons, is considered as the initial state of

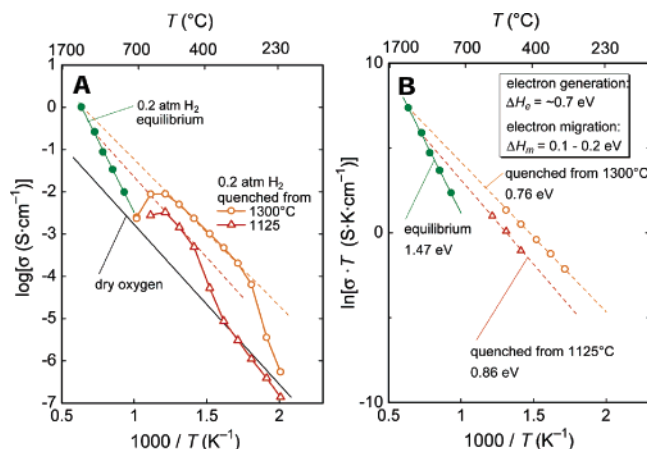


Figure 3. Electrical conductivity of C12A7 for high-temperature equilibrium and for the quenched states. (A) The filled green circles show the equilibrium conductivity in 0.2 atm H_2 atmosphere. Electrical conductivities of samples equilibrated in a hydrogen atmosphere at 1300°C (orange circles) and 1125°C (red triangles) and then quenched are shown. The conductivities were recorded during heating from room temperature in a hydrogen atmosphere. Dashed lines are extrapolations of linear conductivity characteristics of the quenched samples to higher temperatures where they match the high-temperature equilibrium conductivity measured at the respective quenching temperatures. (B) Arrhenius plots of the electronic conductivities. The activation energy for the electronic conductivity of the quenched sample is given by the summation of the electron migration enthalpy of $0.1\text{--}0.2\text{ eV}$ and electron generation enthalpy of $\sim 0.7\text{ eV}$. Since the apparent activation energy for the equilibrium conductivity at the high temperature is 1.47 eV , an extra energy of $\sim 0.7\text{ eV}$ ($= 1.47$ to $\sim 0.1\text{--}0.7$) is required to match this value.

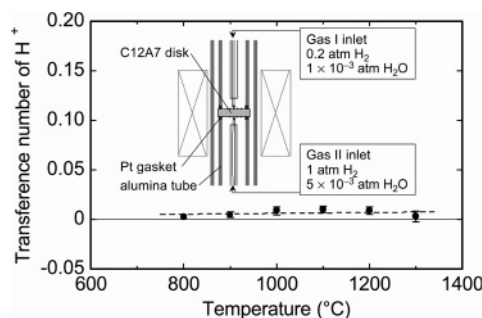
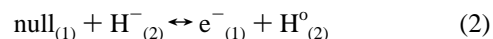


Figure 4. Proton transference number as a function of temperature. The inset shows the experimental setup. Cell voltage between both compartments was converted to the proton transference number. The error bars indicate the experimental error estimated by the reversal of feeding gases to two compartments.

the electron generation reaction. To identify possible final states as well as viable mechanisms for the electron generation, one has to consider the thermal ionization of H^- involving the transfer of a single electron from H^- to the empty neighboring cage as the most evident step:



where “null” denotes the empty cage and subscripts identify different cages. The results of our calculations indicate that the difference in the total energies between the initial and final states in reaction 2 is 3.5 eV , which is much higher than the observed ΔH_{e} of $\sim 0.7\text{ eV}$. Thus, thermal ionization alone cannot explain the experimental results. However, if the H^0 atom, produced in this ionization step, diffuses through the C12A7 lattice and reacts with an extraframework O^{2-} , an extraframework OH^- and another electron are formed. The energy gain in this second reaction step goes up to $\sim 2.5\text{ eV}$. Thus we suggest that the

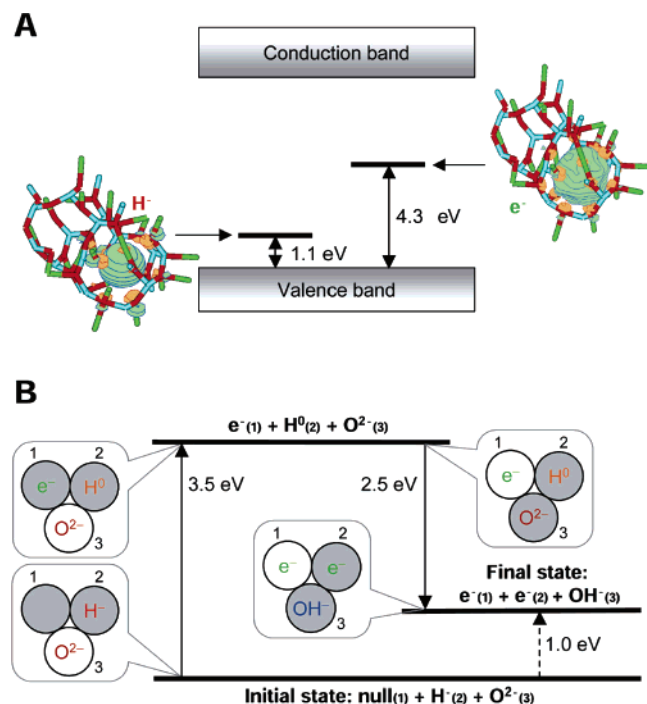
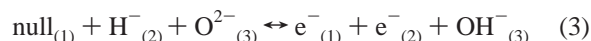


Figure 5. Theoretical calculation of hydrogen species in C12A7. (A) Energy level of the C12A7:e⁻ and C12A7:H⁻ systems calculated using an embedded cluster technique and B3LYP density functional. The iso-surfaces of the one-electron functions for an e⁻ and an H⁻ ion localized in cages are shown. (B) An energy diagram for internal reactions of extraframework species. The illustrations schematically show the cages and incorporated anions. Cages indicated by filled circles were considered in the two cage embedded cluster to evaluate the energy difference between the three states. The ionization of H⁻ requires 3.5 eV. The reaction of the H⁰ with an extraframework O²⁻ results in an energy gain of nearly 2.5 eV. Consequently, the total energy difference between null + H⁻ + O²⁻ and 2e⁻ + OH⁻ is as small as 1.0 eV.

conduction electrons are generated in the following reaction between an extraframework O²⁻ and H⁻:



i.e., two electrons are generated via conversion of the H⁻ ion to an H⁺. As summarized in Figure 5B, the energy difference between the initial and the final states of reaction 3 is found to be ~1 eV. We note that each of the two steps of the mechanism described above involves extraframework species in only two neighboring cages as illustrated in Figure 5B. Therefore it is sufficient to use the 2-cage QM cluster for these calculations.

Discussion

Electron Generation from H⁻ Ion by Thermal Activation.

In the previous sections, the absence of direct intercage H⁻ conduction was demonstrated both experimentally and theoretically. The high electrical conduction observed in both equilibrium and quenched states were ascribed to intercage hopping of electrons. Here we consider activation energy, $\Delta H_e = \sim 0.7$ eV, for the thermal electron generation at <600 °C.

The theoretical calculations suggested that the most plausible thermal electron generation process is reaction 3. The equilibrium constant for this reaction is given by:

$$K_3 = \frac{n^2[\text{OH}^{-}]}{[\text{H}^{-}][\text{null}][\text{O}^{2-}]} \quad (4)$$

where n and square brackets denote the cage-site occupancy of

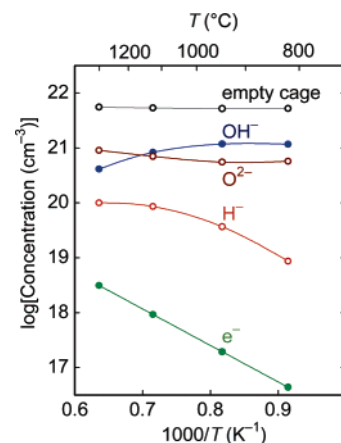


Figure 6. Temperature dependence of equilibrium concentrations of extraframework anions and empty cages in the atmosphere with $p(\text{H}_2) = 0.2$ atm and $p(\text{H}_2\text{O}) = 5 \times 10^{-4}$ atm.

carrier electrons and extraframework chemical species, respectively. Consequently, the temperature dependence of electron content is described as:

$$n = \exp\left(\frac{\Delta S_3}{2k}\right) \left(\frac{[\text{H}^{-}][\text{null}][\text{O}^{2-}]}{[\text{OH}^{-}]}\right)^{1/2} \exp\left(-\frac{\Delta H_3}{2kT}\right) \quad (5)$$

where ΔH_3 and ΔS_3 are the enthalpy and the entropy changes for reaction 3, k is the Boltzmann constant, and T is the absolute temperature. Since the apparent activation energy in eq 4 is given by $\Delta H_3/2$, the experimental results give 1.4 eV as a value of ΔH_3 from the apparent activation energy, $\Delta H_e = 0.7$ eV, for the carrier electron generation. This value agrees reasonably well with theoretically evaluated value of ~1 eV. Thus, we conclude that the carrier electrons are generated thermally via reaction 3 rather than by the single ionization of an H⁻ ion alone.

High-Temperature and Low-Temperature Equilibrium.

As for the high-temperature conductivity at 1300–800 °C, activation energy, ΔH_h , is ~1.5 eV, which is larger than ΔH_q by ~0.7 eV. The preexponential factor, $([\text{H}^{-}][\text{null}][\text{O}^{2-}]/[\text{OH}^{-}])^{1/2}$, in eq 4 could contribute to the extra activation energy, because a relatively rapid equilibration with the atmosphere at high temperatures dynamically changes the concentration of anionic species in the cages. It follows that the higher equilibration temperature is expected to enhance the formation of H⁻ and O²⁻ ions in the cages and suppresses the OH⁻ ion, thereby enhancing the electron generation by thermal activation in the corresponding quenched state.

To substantiate the above expectation, we estimated the temperature dependence of concentrations of extraframework species relevant to the preexponential factor. Here, defects in the lattice framework are ignored, since their concentrations are expected to be very small as compared with those of extraframework species. The electron concentration was evaluated from the observed electrical conductivity assuming that the temperature dependence of the electron mobility is $\mu = (\mu_0/T) \exp(-0.15 \text{ eV}/kT)$ and $\mu = 0.1 \text{ cm}^2\text{s}^{-1}\text{V}^{-1}$ at 300 K.^{11,26} Concentrations of other species were calculated on the following assumptions: (a) the total negative charge density of extraframework O²⁻, OH⁻, H⁻, and e⁻ is equal to the total positive charge density of the lattice framework ($2.3 \times 10^{21} \text{ cm}^{-3}$); (b) the H⁻ concentration is $1 \times 10^{20} \text{ cm}^{-3}$ at 1300 °C; and (c) the preexponential factor $([\text{H}^{-}][\text{null}][\text{O}^{2-}]/[\text{OH}^{-}])^{1/2}$ has an activation energy of 0.7 eV. The results of these calculations, summarized in Figure 6, indicating that the concentrations of O²⁻,

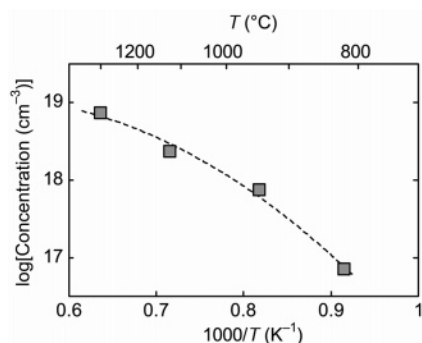


Figure 7. Equilibration temperature dependence of UV-induced extraframework electron concentration. Samples were annealed in the atmosphere with $p(\text{H}_2) = 0.2$ atm and $p(\text{H}_2\text{O}) = 5 \times 10^{-4}$ atm, then quenched to room temperature. UV-light was irradiated at room temperature.

H^- , and electrons increase with temperature to compensate for the decrease in the OH^- concentration. Such a temperature dependence is validated by analogy to the CaO system: annealing of CaO in a hydrogen atmosphere results in the incorporation of traces of H^- and OH^- ions as well as electrons (F^+ centers) at O^{2-} ion sites.⁶ A thermodynamic calculation⁴² of the CaO system in a hydrogen atmosphere also demonstrated that the thermodynamic activity for H^- and electrons increases while that of OH^- decreases with increasing temperature.

Figure 7 shows the concentration of the extraframework electrons generated by the UV-irradiation at room temperature against equilibration temperature of the hydrogen treatment. The electron concentration increases with the equilibration temperature, indicating the equilibrium H^- concentration increases with temperature. This tendency is consistent with the temperature dependence of H^- concentration in Figure 6.

The chemical composition established at high temperatures (Figure 6) is preserved by the rapid quenching to temperatures lower than ~ 600 °C. In this temperature range, neither in-diffusion of atmospheric species nor out-diffusion of extraframework species is virtually forbidden during a time-scale of the experiments, and hence only the reactions among the extraframework species are allowed. Reaction 3 describes such an internal equilibrium. Since its enthalpy change is positive, the chemical equilibrium moves to the left with decreasing temperature. Consequently, electrons are annihilated by the reaction with OH^- to form H^- and O^{2-} ions as the temperature decreases, leading to the lower conductivity at the lower temperature. Finally the C12A7 becomes insulating at room temperature.¹¹ In other words, the OH^- ions remaining in the high-temperature equilibrium act as scavengers of carrier electrons. The detailed mechanism of this reaction will be discussed elsewhere.⁴³ If the electron concentration in the high-temperature equilibrium is twice as large as that of OH^- ions, electrons can still survive in the lower temperature equilibrium and then a considerable electronic conductivity should appear even at room temperature. Such a situation is realized in OH^- -ion-bearing C12A7 films implanted with inert gas ions to high fluences.⁴⁴ The internal equilibrium forces concentrations of H^- and OH^- to increase, while the concentration of O^{2-} decreases with decreasing temperature. Interestingly, these trends are opposite to those observed in Figure 6. The difference is ascribed to whether the atmosphere is involved with the formation of extraframework species or not.

H_2 Desorption. When the quenched C12A7 was again heated over 600 °C in the helium atmosphere, a strong H_2 desorption was observed. In this temperature range, reactions of atmo-

spheric species with the extraframework species proceed. The H_2 desorption should be caused as a result of change in the chemical composition established at the high temperature (1300 °C) in the hydrogen atmosphere to the new equilibrium states established under different temperature (600 °C) and atmospheric (helium) conditions. In the previous study,¹¹ the desorption process has been ascribed to reaction 1a. This process accompanies annihilation of extraframework OH^- ions. However, as shown in Figure 6, formation of OH^- is rather favored in the temperature range of the H_2 desorption. In addition, according to thermodynamic study on the OH^- formation in C12A7, the dehydration at 600 °C requires $p(\text{H}_2\text{O})$ less than 1×10^{-7} atm. Such a low $p(\text{H}_2\text{O})$ was probably not attained in the current experiment, because the helium gas flowing in a furnace empirically contains H_2O with more than 10^{-6} atm. Formation of extraframework electrons by the H_2 desorption is also ruled out, because electron concentration in the new equilibrium states is negligibly small; equilibrium electron concentration at 600 °C expected from Figure 6 is less than $1 \times 10^{15} \text{ cm}^{-3}$ even in the hydrogen atmosphere. Thus, the H_2 desorption involves the formation of the extraframework OH^- ions. Consequently, reaction 1c is most likely as the dominant process for the H_2 desorption.

Persistence of the Light-Induced or Electron Beam-Induced Electrons. Although the internal equilibration at the lower temperature makes the hydrogen-treated C12A7 insulating, exposure of the hydrogen-treated C12A7 to UV-light or electron beam converts it to an electronic conductor. The electronic conductivity persists without any apparent degradation at room temperature for more than a few years after the irradiation. On the contrary, when the conductive sample is heated to temperatures over ~ 300 °C the inversion to the insulating state is completed within several minutes.¹¹ Thus, the electronic conductive state is a meta-stable state. Quite large temperature dependence of the inversion kinetics suggests the presence of a high potential barrier for the inversion process, which effectively stabilizes the conductive state. In the previous study,¹¹ the stabilization process was tentatively ascribed to formation of H_2 molecule in the cage from two photodissociated H° atoms. A recent theoretical study evaluates energy gain for this process as 3.5 eV,⁴³ thus 1.75 eV is assigned to the energy gain per one H° atom. As demonstrated in the results section, if the H° atom reacts with an extraframework O^{2-} to form an extraframework OH^- and an electron, 2.5 eV is obtained as the energy gain. Thus, the latter process is more feasible in terms of the stability. Moreover, the H_2 formation is less likely if one considers probable concentration of H° atoms in comparison with concentration of other extraframework species. Concentration of extraframework O^{2-} ions ($\sim 10^{21} \text{ cm}^{-3}$, see Figure 6) in the hydrogen-treated C12A7 is at least 2 orders of magnitude larger than that of electrons ($< 10^{19} \text{ cm}^{-3}$, see Figure 7) generated by UV irradiation. If H° atoms recombine to form H_2 molecules, the electron concentration is the same as the total concentration of H° formed by the irradiation. Alternatively, in the case of the H° reaction with extraframework O^{2-} and formation of an OH^- and an electron, the electron concentration is twice that of the H° . In both cases, the total H° concentration is far smaller than that of the extraframework O^{2-} ions. Thus, H° atoms have little chance to diffuse to form H_2 molecules before being trapped by the O^{2-} ions.

Consequently we suggest that reaction 3 holds for the light- or electron beam-induced generation of carrier electrons as well as the thermal one. According to this scheme, the persistence of the carrier electrons generated by the irradiation at room

temperature necessitates the extraframework O^{2-} ions. As observed in Figure 6, the equilibrium O^{2-} concentration increases with temperature. Thus, this tendency is also consistent with the fact that higher equilibration temperature enhances the UV-light-induced carrier electron generation at room temperature (Figure 7).

Concluding Remarks

The presence of H^- ions in C12A7 cages is crucial for the pronounced electrical conductivity, which exceeds the fast oxide ion conductivity in C12A7. However, intercage migration of the H^- ions is not a dominant conduction process. Instead, the dominant charge carriers are electrons generated from the H^- ions by thermal excitation. Due to the marked instability of H^0 , the release of a single electron from an H^- does not constitute the complete reaction process for the electron generation. The complete process involves the release of two electrons via the reaction of an H^- ion with an O^{2-} ion in a cage with the formation of an OH^- ion. Thus, the H^- ion in C12A7 acts as a two-electron donor via the conversion from an H^- to an H^+ charge state. A higher equilibration temperature raises the concentration of H^- and O^{2-} ions in cages, thereby enhancing the electron generation by thermal activation in the corresponding quenched state. In addition, the formation of OH^- ions by the reaction H^- and O^{2-} ions also explains well the persistence of the UV-induced carrier electrons.

The present study reveals that the H^- ion in C12A7 acts as a two-electron donor via conversion of H^- to H^+ . It should be noted that the hydrogen differs from a conventional donor center in that the electron capture and release processes are accompanied by migration and chemical reaction, leading to a unique response to thermal or light excitation, such as the persistence of carrier electrons formed by the UV irradiation at room temperature. As found in the C12A7 system, incorporation of H^- ions into the nanostructure of various oxides may provide a new approach for imparting the unique nature of hydrogen to these materials.

Acknowledgment. The authors thank L. Skuja and C. Bird for reading the manuscript. This work was supported by the Grant-in-Aid for Creative Scientific Research (No.16GS0205) from the Japanese Ministry of Education, Culture, Sports, Science and Technology. The HPCx computer time was awarded to the Materials Chemistry consortium under EPSRC grant GR/S13422/01.

References and Notes

- (1) Van de Walle, C. G.; Neugebauer, J. *Nature* **2003**, *423*, 626–628.
- (2) Kreuer, K. D. *Solid State Ionics* **2000**, *136–137*, 149–160.
- (3) Beyer, W. *Tetrahedrally-Bonded Amorphous Semiconductors*; Adler, D., Fritzsche, H., Eds.; Plenum Press: New York, 1985; p 129.
- (4) Sandrock, G. *J. Alloys. Comput.* **1999**, *293–295*, 877–888.
- (5) Cotton, F. A.; Wilkinson, G. *Advanced Inorganic Chemistry*, 5th ed.; Wiley: New York, 1988.
- (6) González, R.; Chen, Y. *J. Phys.: Condens. Matter* **2002**, *14*, R1143–R1173.
- (7) Diwald, O.; Hofmann, P.; Knözinger, E. *Phys. Chem. Chem. Phys.* **1999**, *1*, 713–721.
- (8) Paganini, M. C.; Chiesa, M.; Giamello, E.; Coluccia, S.; Martra, G.; Murphy, D. M.; Pacchioni, G. *Surf. Sci.* **1999**, *421*, 246–262.
- (9) Poulsen, F. W. *Solid State Ionics* **2001**, *145*, 387–397.
- (10) Hayward, M. A.; Cussen E. J.; Claridge, J. B.; Bieringer, M.; Rosseinsky, M. J.; Kiely, C. J.; Blundell, S. J.; Marshall, I. M.; Pratt, F. L. *Science* **2002**, *295*, 1882–1884.
- (11) Hayashi, K.; Matsuishi, S.; Kamiya, T.; Hirano, M.; Hosono, H. *Nature* **2002**, *419*, 462–465.
- (12) Hayashi, K.; Toda, Y.; Kamiya, T.; Hirano, M.; Yamanaka, M.; Tanaka, I.; Yamamoto, T.; Hosono, H. *Appl. Phys. Lett.* **2005**, *86*, 022109–1–3.
- (13) Huang, F.; Li, J.; Wang, L.; Dong, T.; Tu, J.; Torimoto, Y.; Sadakata, M.; Li, Q. *J. Phys. Chem. B* **2005**, *109*, 12032–12037.
- (14) Norby, T.; Larring, Y. *Solid State Ionics* **2000**, *136–137*, 139–148.
- (15) Norby, T.; Widerøe, M.; Glöckner, R.; Larring, Y. *Dalton Trans.* **2004**, 3012–3018.
- (16) Bartl, H.; Scheller, T. *N. Jb. Miner. Mh.* **1970**, *35*, 547–552.
- (17) Jeevaratnam, J.; Glasser, F. P.; Glasser, L. S. D. *J. Am. Ceram. Soc.* **1964**, *47*, 105–106.
- (18) Zhmoidin, G. I.; Chatterjee, A. K. *Cem. Concr. Res.* **1984**, *14*, 386–396.
- (19) Hosono, H.; Abe, Y. *Inorg. Chem.* **1987**, *26*, 1192–1195.
- (20) Hayashi, K.; Hirano, M.; Matsuishi, S.; Hosono, H. *J. Am. Chem. Soc.* **2002**, *124*, 738–739.
- (21) Hayashi, K.; Matsuishi, S.; Ueda, N.; Hirano, M.; Hosono, H. *Chem. Mater.* **2003**, *15*, 1851–1854.
- (22) Hayashi, K.; Matsuishi, S.; Hirano, M.; Hosono, H. *J. Phys. Chem. B* **2004**, *108*, 8920–8925.
- (23) Hayashi, K.; Ueda, N.; Hirano, M.; Hosono, H. *Solid State Ionics* **2004**, *173*, 89–94.
- (24) Matsuishi, S.; Hayashi, K.; Hirano, M.; Tanaka, I.; Hosono, H. *J. Phys. Chem. B* **2004**, *108*, 18557–18568.
- (25) Hayashi, K.; Hirano, M.; Hosono, H. *Chem. Lett.* **2005**, *34*, 586–587.
- (26) Matsuishi, S.; Toda, Y.; Miyakawa, M.; Hayashi, K.; Kamiya, T.; Hirano, H.; Hosono, H. *Science* **2003**, *301*, 626–629.
- (27) Sushko, P. V.; Shluger, A. L.; Hayashi, K.; Hirano, M.; Hosono, H. *Phys. Rev. Lett.* **2003**, *91*, 126401–4.
- (28) Sushko, P. V.; Shluger, A. L.; Hayashi, K.; Hirano, M.; Hosono, H. *Thin Solid Films* **2003**, *445*, 161–167.
- (29) Lacerda, M.; Irvine, J. T. S.; Glasser, F. P.; West, A. R. *Nature* **1988**, *332*, 525–526.
- (30) Sushko, P. V.; Shluger, A. L.; Hayashi, K.; Hirano, M.; Hosono, H. *Phys. Rev. B*, in press.
- (31) Imlach, J. A.; Glasser, L. S. D.; Glasser, F. P. *Cem. Concr. Res.* **1971**, *1*, 57–61.
- (32) Hayashi, K.; Hirano, M.; Hosono, H. *J. Phys. Chem. B* **2005**, *109*, 11900–11906.
- (33) Miyakawa, M.; Hayashi, K.; Hirano, M.; Toda, Y.; Kamiya, T.; Hosono, H. *Adv. Mater.* **2003**, *15*, 1100–1103.
- (34) Sushko, P. V.; Shluger, A. L.; Hayashi, K.; Hirano, M.; Hosono, H. *Appl. Phys. Lett.* **2005**, *86*, 092101–1–3.
- (35) Matsuishi, S.; Hayashi, K.; Hirano, M.; Hosono, H. *J. Am. Chem. Soc.* **2005**, *127*, 12454–12455.
- (36) Hayashi, K.; Hirano, M.; Hosono, H. *J. Mater. Res.* **2002**, *17*, 1244–1247.
- (37) Watauchi, S.; Tanaka, I.; Hayashi, K.; Hirano, M.; Hosono, H. *J. Cryst. Growth* **2002**, *237–239*, 801–805.
- (38) Sushko, P. V.; Shluger, A. L.; Catlow, C. R. A. *Surf. Sci.* **2000**, *450*, 153–170.
- (39) Sulimov, V. B.; Sushko, P. V.; Edwards, A. H.; Shluger, A. L.; Stoneham, A. M. *Phys. Rev. B* **2002**, *66*, 024108–1–14.
- (40) Frisch, M. J.; Trucks, G. W.; Schlegel, H. B.; Scuseria, G. E.; Robb, M. A.; et al. *Gaussian 98*, revision A7; Gaussian Inc.: Pittsburgh, PA, 1998.
- (41) Lacerda, M.; West, A. R.; Irvine, J. T. S. *Solid State Ionics* **1993**, *59*, 257–262.
- (42) Calculated using Malt program, Kagaku Gijutsu-Sha, Japan; Yokokawa, H.; Yamauchi, S.; Matsumoto, T. *Calphad* **2002**, *26*, 155–166.
- (43) Sushko, P. V.; Shluger, A. L.; Hayashi, K.; Hirano, M.; Hosono, H. Submitted for publication.
- (44) Miyakawa, M.; Toda, Y.; Hayashi, K.; Kamiya, T.; Hirano, M.; Hosono, H. *J. Appl. Phys.* **2005**, *92*, 023510–1–6.